vHeat: Building Vision Models upon Heat Conduction

Zhaozhi Wang[1,2]*, Yue Liu[1]*, Yunfan Liu[1] , Hongtian Yu[1],
Yaowei Wang[2,3] , Qixiang Ye[1,2] , Yunjie Tian[1]
[1]University of Chinese Academy of Sciences   [2]Peng Cheng Laboratory
[3]Harbin Institute of Technology (Shenzhen)
wangzhaozhi22@mails.ucas.ac.cn   liuyue171@mails.ucas.ac.cn
yunfan.liu@ucas.ac.cn   yuhongtian17@mails.ucas.ac.cn
wangyw@pcl.ac.cn   qxye@ucas.ac.cn   tianyunjie19@mails.ucas.ac.cn

Abstract

A fundamental problem in learning robust and expressive visual representations lies in efficiently estimating the spatial relationships of visual semantics throughout the entire image. In this study, we propose vHeat, a novel vision backbone model that simultaneously achieves both high computational efficiency and global receptive field. The essential idea, inspired by the physical principle of heat conduction, is to conceptualize image patches as heat sources and model the calculation of their correlations as the diffusion of thermal energy. This mechanism is incorporated into deep models through the newly proposed module, the Heat Conduction Operator (HCO), which is physically plausible and can be efficiently implemented using DCT and IDCT operations with a complexity of $\mathcal{O}(N^{1.5})$. Extensive experiments demonstrate that vHeat surpasses Vision Transformers (ViTs) across various vision tasks, while also providing higher inference speeds, reduced FLOPs, and lower GPU memory usage for high-resolution images. The code will be released at https://github.com/MzeroMiko/vHeat and https://openi.pcl.ac.cn/georgew/vHeat.

1 Introduction

Convolutional Neural Networks (CNNs) [26, 21] have been the cornerstone of visual representation since the advent of deep learning, exhibiting remarkable performance across vision tasks. However, the reliance on local receptive fields and fixed convolutional operators imposes constraints, particularly in capturing long-range and complex dependencies within images [36]. These limitations have motivated significant interest in developing alternative visual representation models, including architectures based on ViTs [16, 32] and State Space Models [67, 30]. Despite their effectiveness, these models continue to face challenges, including relatively high computational complexity and a lack of interpretability.

When addressing these limitations, we draw inspiration from the field of heat conduction, where *spatial locality* is crucial for the transfer of thermal energy due to the collision of neighboring particles. Notably, analogies can be drawn between the principles of heat conduction and the propagation of visual semantics within the spatial domain, as adjacent image regions in a certain scale tend to contain related information or share similar characteristics. Leveraging these connections, we introduce **vHeat**, a physics-inspired vision backbone model that conceptualizes image patches as *heat sources* and models the calculation of their correlations as the diffusion of thermal energy.

To integrate the principle of heat conduction into deep networks, we first derive the general solution of heat conduction in 2D space and extend it to multiple dimensions, corresponding to various feature channels. Based on this general solution, we design the **Heat Conduction Operator (HCO)**,
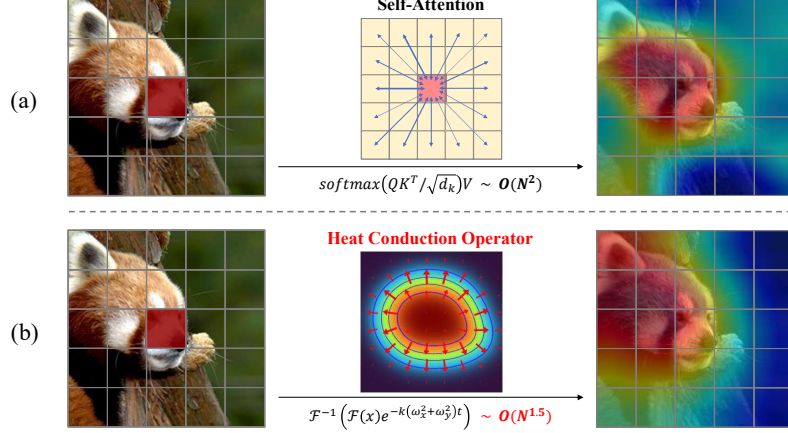
---

*Equal contribution.

Figure 1: Comparison of information conduction mechanisms: self-attention *vs.* heat conduction. (a) The self-attention operator uniformly "conducts" information from a pixel to all other pixels, resulting in $\mathcal{O}(N^2)$ complexity. (b) The heat conduction operator (HCO) conceptualizes the center pixel as the heat source and conducts information propagation through DCT ($\mathcal{F}$) and IDCT ($\mathcal{F}^{-1}$), which enjoys interpretability, global receptive fields, and $\mathcal{O}(N^{1.5})$ complexity.

which simulates the propagation of visual semantics across image patches along multiple dimensions. Notably, we demonstrate that HCO can be approximated through 2D DCT and IDCT operations, effectively reducing the computational complexity to $\mathcal{O}(N^{1.5})$. This improvement boosts both training and testing efficiency due to the high parallelizability of DCT and IDCT operations. Furthermore, as each element in the frequency domain obtained by DCT incorporates information from all patches in the image space, vHeat can establish long-range feature dependencies and achieve global receptive fields. To enhance the representation adaptability of vHeat, we propose learnable frequency value embeddings (FVEs) to characterize the frequency information and predict the thermal diffusivity of visual heat conduction.

We develop a family of vHeat models (*i.e.*, vHeat-Tiny/Small/Base), and extensive experiments are conducted to demonstrate their effectiveness in diverse visual tasks. Compared to benchmark vision backbones with various architectures (*e.g.*, ConvNeXt [33], Swin [32], and Vim [67]), vHeat consistently achieves superior performance on image classification, object detection, and semantic segmentation across model scales. Specifically, vHeat-Base achieves a 83.9% top-1 accuracy on ImageNet-1K, surpassing Swin by 0.4%, with a throughput exceeding that of Swin by a substantial margin over 40% (661 *vs.* 458). Besides, due to the $\mathcal{O}(N^{1.5})$ complexity of HCO, vHeat enjoys considerably lower computational cost compared to ViT-based models, demonstrating significantly reduced FLOPs and GPU memory requirements, and higher throughput as image resolution increases. In particular, when the input image resolution increases to 768×768, vHeat-Base achieves a $3\times$ throughput compared to Swin, with over 70% less GPU memory allocation and more than 30% fewer computational FLOPs.

The contributions of this study are summarized as follows:

- We propose vHeat, a vision backbone model inspired by the physical principle of heat conduction, which simultaneously achieves global receptive fields, low computational complexity, and high interpretability.

- We design the Heat Conduction Operator (HCO), a physically plausible module conceptualizing image patches as heat sources, predicting adaptive thermal diffusivity by FVEs, and transferring information following the principles of heat conduction.

- Without bells and whistles, vHeat achieves promising performance in vision tasks including image classification, object detection, and semantic segmentation. It also enjoys higher inference speeds, reduced FLOPs, and lower GPU memory usage for high-resolution images.

2 Related Work

Convolution Neural Networks. CNNs have been landmark models in the history of visual perception [27, 26]. The distinctive characteristics of CNNs are encapsulated in the convolution kernels, which enjoy high computational efficiency given specifically designed GPUs. With the aid of powerful GPUs and large-scale datasets [12], increasingly deeper [43, 48, 21, 25] and efficient models [23, 49, 63, 40] have been proposed for higher performance across a spectrum of vision tasks. Numerous modifications have been made to the convolution operators to improve its capacity [8], efficiency [24, 64] and adaptability [9, 57]. Nevertheless, the born limitation of local receptive fields remains. Recently developed large convolution kernels [14] took a step towards large receptive fields, but experienced difficulty in handling high-resolution images.

Vision Transformers. Built upon the self-attention operator [54], ViTs have the born advantage of building global feature dependency. Based on the learning capacity of self-attention across all image patches, ViTs has been the most powerful vision model ever, given a large dataset for pre-training [16, 52, 39]. The introduction of hierarchical architectures [32, 15, 58, 35, 65, 51, 10, 13, 66] further improves the performance of ViTs. The Achilles' Heel of ViTs is the $\mathcal{O}(N^2)$ computational complexity, which implies substantial computational overhead given high-resolution images. Great efforts have been made to improve model efficiency by introducing window attention, linear attention and cross-covariance attention operators [56, 32, 4, 1], at the cost of reducing receptive fields or non-linearity capacity. Other studies proposed hybrid networks by introducing convolution operations to ViTs [59, 10, 53], designing hybrid architectures to combine CNN with ViT modules [10, 45, 35].

State Space Models and RNNs. State space models (SSMs) [20, 37, 55], which have the long-sequence modeling capacity with linear complexity, are also migrated from the natural language area (Mamba [19]). Visual SSMs were also designed by adapting the selective scan mechanism to 2-D images [67, 30]. Nevertheless, SSMs built upon the selective scan mechanism lack the advantages of high parallelism, which limit its potential.

Recent receptance weighted key value (RWKV) and RetNet models [38, 47] improved the parallelism while retaining the linear complexity. They combine the efficient parallelizable training of transformers with the efficient inference of RNNs, leveraging a linear attention mechanism and allowing formulation of the model as either a Transformer or an RNN, thus parallelizing computations during training and maintaining constant computational and memory complexity during inference. Despite the advantages, modeling a 2-D image as a sequence impairs interpretability.

Biology and Physics Inspired Models. Biology and physics principles have long been the fountainhead of creating vision models. Diffusion models [44, 22, 42], motivated by Nonequilibrium thermodynamics [11], are endowed with the ability to generate images by defining a Markov chain for the diffusion step. QB-Heat [6] utilizes physical heat equation as supervision signal for masked image modeling task. Spiking Neural Network (SNNs) [18, 50, 28] claims better simulation on the information transmission of biological neurons, formulating models for simple visual tasks [2]. The success of these models encourages us to explore the principle of physical heat conduction for the development of vision representation models.

3 Methodology

3.1 Preliminaries: Physical Heat Conduction

Let $u(x, y, t)$ denote the temperature of point (x, y) at time t within a two-dimensional region $D \in \mathbb{R}^2$, the classic physical heat equation [60] can be formulated as

$$\frac{\partial u}{\partial t} = k \left(\frac{\partial^2 u}{\partial x^2} + \frac{\partial^2 u}{\partial y^2} \right), \tag{1}$$

where $k > 0$ is the **thermal diffusivity** [3] measuring the rate of heat transfer in a material. By setting the initial condition $u(x, y, t)|_{t=0}$ to $f(x, y)$, the general solution of Eq. (1) can be derived by applying the Fourier Transform (FT, denoted as $\mathcal{F}$) to both sides of the equation, which gives

$$\mathcal{F} \left(\frac{\partial u}{\partial t} \right) = k \mathcal{F} \left(\frac{\partial^2 u}{\partial x^2} + \frac{\partial^2 u}{\partial y^2} \right). \tag{2}$$
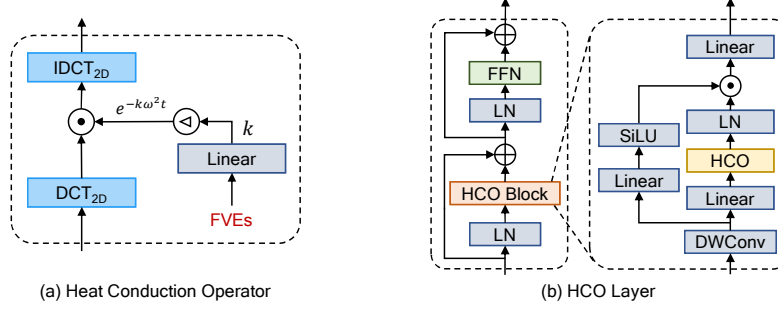
(a) Heat Conduction Operator

(b) HCO Layer

Figure 2: HCO and HCO layer. FVEs, FFN, LN, DWConv respectively denote frequency value embeddings, feed-forward network, layer normalization, and depth-wise convolution[3].

Denoting $\widetilde{u}(\omega_x, \omega_y, t)$ as the FT-transformed form of $u(x, y, t)$, *i.e.*, $\widetilde{u}(\omega_x, \omega_y, t) \coloneqq \mathcal{F}(u(x, y, t))$, the left-hand-side of Eq. (2) can be written as

$$\mathcal{F}\left(\frac{\partial u}{\partial t}\right) = \frac{\partial \widetilde{u}(\omega_x, \omega_y, t)}{\partial t}. \tag{3}$$

and by leveraging the derivative property of FT, the right-hand-side of Eq. (2) can be transformed as

$$\mathcal{F}\left(\frac{\partial^2 u}{\partial x^2} + \frac{\partial^2 u}{\partial y^2}\right) = -(\omega_x^2 + \omega_y^2)\widetilde{u}(\omega_x, \omega_y, t). \tag{4}$$

Therefore, by combining the expression of both sides of the equation, Eq. (2) can be formulated as an ordinary differential equation (ODE) in the frequency domain, which can be written as

$$\frac{d\widetilde{u}(\omega_x, \omega_y, t)}{dt} = -k(\omega_x^2 + \omega_y^2)\widetilde{u}(\omega_x, \omega_y, t). \tag{5}$$

By setting the initial condition $\widetilde{u}(\omega_x, \omega_y, t)|_{t=0}$ to $\widetilde{f}(\omega_x, \omega_y)$ ($\widetilde{f}(\omega_x, \omega_y)$ denotes the FT-transformed $f(x, y)$), $\widetilde{u}(\omega_x, \omega_y, t)$ in Eq (5) can be solved as

$$\widetilde{u}(\omega_x, \omega_y, t) = \widetilde{f}(\omega_x, \omega_y)e^{-k(\omega_x^2 + \omega_y^2)t}. \tag{6}$$

Finally, the general solution of heat equation in the spatial domain can be obtained by performing inverse Fourier Transformer ($\mathcal{F}^{-1}$) on Eq. (6), which gives the following expression

$$u(x, y, t) = \mathcal{F}^{-1}(\widetilde{f}(\omega_x, \omega_y)e^{-k(\omega_x^2 + \omega_y^2)t}) \tag{7}$$

$$= \frac{1}{4\pi^2}\int_{\widetilde{D}}\widetilde{f}(\omega_x, \omega_y)e^{-k(\omega_x^2 + \omega_y^2)t}e^{i(\omega_x x + \omega_y y)}d\omega_x d\omega_y. \tag{8}$$

3.2 vHeat: Visual Heat Conduction

Drawing inspiration from the analogies between the principles of physical heat conduction and the propagation of visual semantics within the spatial domain (*i.e.*, 'visual heat conduction'), we propose **vHeat**, a physics-inspired deep architecture for visual representation learning. The vHeat model is built upon the Heat Conduction Operator (HCO), which is designed to integrate the principle of heat conduction into handling the discrete feature of vision data. We also leverage the thermal diffusivity in the classic physical heat equation (Eq (1)) to improve the adaptability of vHeat to vision data.

3.2.1 Heat Conduction Operator (HCO)

To extract visual features, we design HCO to implement the conduction of visual information across image patches in multiple dimensions, following the principle of physical heat conduction. To this end, we first extend the 2D temperature distribution $u(x, y, t)$ along the channel dimension and

---

[3]Please refer to Sec. E.3 in Appendix, where we demonstrate that while depth-wise convolution aids in feature extraction, the primary improvements are attributed to the proposed HCO.
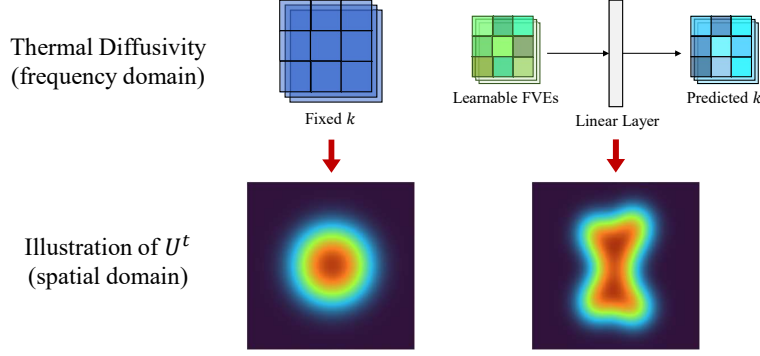
Figure 3: Illustration of temperature distribution U^t *w.r.t.* thermal diffusivity k, given a heat source as the initial condition. The predicted k leads to nonuniform visual heat conduction, which facilitates the adaptability of visual representation. (Best viewed in color)

denote the resultant multi-channel image feature as $U(x, y, c, t)$ $(c = 1, \cdots, C)$. Mathematically, considering the input as $U(x, y, c, 0)$ and the output as $U(x, y, c, t)$, HCO simulates the general solution of physical heat conduction (Eq. (7)) in visual data processing, which can be formulated as

$$U^t = \mathcal{F}^{-1}(\mathcal{F}(U^0)e^{-k(\omega_x^2 + \omega_y^2)t}), \tag{9}$$

where U^t and U^0 are abbreviations for $U(x, y, c, t)$ and $U(x, y, c, 0)$, respectively.

For applying $\mathcal{F}(\cdot)$ and $\mathcal{F}^{-1}(\cdot)$ to discrete image patch features, it is necessary to utilize the discrete version of the (inverse) Fourier Transform (*i.e.*, DFT and IDFT). However, since vision data is spatially constrained and semantic information will not propagate beyond the border, we additionally introduce a common assumption of Neumann boundary condition [7], *i.e.*, $\partial u(x, y, t)/\partial \mathbf{n} = 0, \forall(x, y) \in \partial D, t \geq 0$, where $\mathbf{n}$ denotes the normal to the image boundary ∂D. As vision data is typically rectangular, this boundary condition enables us to replace the 2D DFT and IDFT with the 2D discrete cosine transformation, $\mathbf{DCT_{2D}}$, and the 2D inverse discrete cosine transformation, $\mathbf{IDCT_{2D}}$ [46]. Therefore, the discrete implementation of HCO can be expressed as

$$U^t = \mathbf{IDCT_{2D}}(\mathbf{DCT_{2D}}(U^0)e^{-k(\omega_x^2 + \omega_y^2)t}), \tag{10}$$

and its internal structure is illustrated in Fig. 2(a). Particularly, the parameter k stands for the thermal diffusivity in physical heat conduction and is predicted based on the features within the frequency domain (explained in the following subsection).

Notably, due to the computational efficiency of $\mathbf{DCT_{2D}}$, the overall complexity of HCO is $\mathcal{O}(N^{1.5})$, where N denotes the number of input image patches. Please refer to Sec. B in Appendix for the detailed implementation of HCO using $\mathbf{DCT_{2D}}$ and $\mathbf{IDCT_{2D}}$.

3.2.2 Adaptive Thermal Diffusivity

In physical heat conduction, thermal diffusivity represents the rate of heat transfer within a material. While in visual heat conduction, we hypothesize that more representative image contents contain more energy, resulting in higher temperatures in the corresponding image features within $U(x, y, c, t)$. Therefore, it is suggested that the thermal diffusivity parameter k should be learnable and adaptive to image content, which facilitates the adaptability of heat condution to visual representation learning.

Given that the output of $\mathbf{DCT}$ (i.e., $\mathbf{DCT_{2D}}(U^0)$ in Eq. (10)) lies in the frequency domain, we also determine k based on frequency values ($k := k(\omega_x, \omega_y)$). Since different positions in the frequency domain correspond to different frequency values, we propose to represent these values using learnable Frequency Value Embeddings (FVEs), which function similarly to the widely used absolute position embeddings in ViTs[16] (despite in the frequency domain). As shown in Figure 2 (a), FVEs are fed to a linear layer to predict the thermal diffusivity k, allowing it to be non-uniform and adaptable to visual representations.

Practically, considering that k and t (the conduction time) are multiplied in Eq. (10), we empirically set a fixed value for t and predict the values of k. Specifically, FVEs are shared within each network stage of vHeat to facilitate the convergence of the training process.
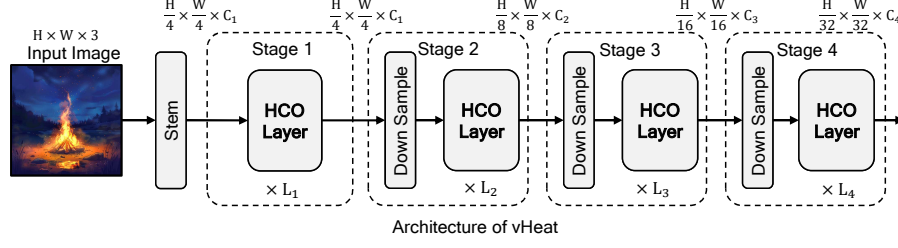
Figure 4: The network architecture of vHeat.

3.2.3 vHeat Model

Network Architecture. We develop a vHeat model family including vHeat-Tiny (vHeat-T), vHeat-Small (vHeat-S), and vHeat-Base (vHeat-B). An overview of the network architecture of vHeat is illustrated in Fig. 4, and the detailed configurations are provided in Sec. C in Appendix. Given an input image with the spatial resolution of $H \times W$, vHeat first partitions it to image patches through a stem module, yielding a 2D feature map with $\frac{H}{4} \times \frac{W}{4}$ resolution. Subsequently, multiple stages are utilized to create hierarchical representations with gradually decreased resolutions of $\frac{H}{4} \times \frac{W}{4}$, $\frac{H}{8} \times \frac{W}{8}$, $\frac{H}{16} \times \frac{W}{16}$ and increasing channels. Each stage is composed of a down-sampling layer followed by multiple heat conduction layers (except for the first stage).

Heat Conduction Layer. The heat conduction layer, Fig. 2 (b), is similar to the ViTs block while replacing self-attention operators with HCOs and retaining the feed-forward network (FFN). It first utilizes a 3×3 depth-wise convolution layer. The depth-wise convolution is followed by two branches: one maps the input to HCO and the other computes the multiplicative gating signal like [30]. HCO plays a crucial role in each heat conduction layer, Fig. 2 (b), where the mapped features from a linear layer are first processed by the $\mathbf{DCT_{2D}}$ operator to generate features in the frequency domain. Additionally, HCO takes FVEs as input for frequency representation to predict adaptive thermal diffusivity k through a linear layer. By multiplying the coefficient matrix $e^{-k\omega^2 t}$ and performing $\mathbf{IDCT_{2D}}$, HCO implements the discrete solution of the visual heat equation, Eq. (10).

3.3 Discussion

• **What is role of the thermal diffusivity coefficient** $e^{-k(\omega_x^2+\omega_y^2)t}$**?** When multiplying with $\mathbf{DCT_{2D}}(U^0)$, $e^{-k(\omega_x^2+\omega_y^2)t}$ acts as an adaptive filter in the frequency domain to perform visual heat conduction. Different frequency values correspond to distinct image patterns, *i.e.*, high frequency corresponds to edges and textures while low frequency corresponds to flat regions. With adaptive thermal diffusivity, HCO can enhance/depress these patterns within each feature channel. Aggregating the filtered features from all channels, vHeat achieves a robust feature representation.

• **Why does temperature** $U(x, y, c, t)$ **correspond to visual features?** Visual features are essentially the outcome of the feature extraction process, characterized by pixel propagation within the feature map. This process aligns with the properties of existing convolution, self-attention, and selective scan operators, exemplifying a form of information conduction. Similarly, visual heat conduction embodies this concept of information conduction through temperature, denoted as $U(x, y, c, t)$.

• **What is the relationship/difference between HCO and self-attention?** HCO dynamically propagates energy via heat conduction, enabling the perception of global information within the input image. This positions HCO as a distinctive form of attention mechanism. The distinction lies in its reliance on interpretable physical heat conduction, in contrast to self-attention, which is formulated through token similarity. Furthermore, HCO works in the frequency domain, implying its potential to affect all image patches through frequency filtering. Consequently, HCO exhibits greater efficiency compared to self-attention, which necessitates computing the relevance of all pairs across image patches.

Table 1: Performance comparison of image classification on ImageNet-1K. Test throughput values are measured with an A100 GPU, using the toolkit released by [61], following the protocol proposed in [32]. The batch size is set as 128, and the PyTorch version is 2.2. Please refer to Sec. D in Appendix for complete comparisons.

Method	Image size	#Param.	FLOPs	Test Throughput (img/s)	ImageNet top-1 acc. (%)
ConvNeXt-T [33]	224^2	29M	4.5G	1198	82.1
ConvNeXt-S [33]	224^2	50M	8.7G	684	83.1
ConvNeXt-B [33]	224^2	89M	15.4G	436	83.8
Swin-T [32]	224^2	28M	4.6G	1244	81.3
Swin-S [32]	224^2	50M	8.7G	718	83.0
Swin-B [32]	224^2	88M	15.4G	458	83.5
vHeat-T	224^2	29M	4.6G	1514	82.2
vHeat-S	224^2	50M	8.5G	945	83.6
vHeat-B	224^2	87M	14.9G	661	83.9

Table 2: **Left**: Results of object detection and instance segmentation on COCO dataset. FLOPs are calculated with input size 1280×800. AP^b and AP^m denote box AP and mask AP, respectively. The notation '1×' indicates models fine-tuned for 12 epochs, while '3×MS' denotes the utilization of multi-scale training for 36 epochs. **Right**: Results of semantic segmentation on ADE20K using UperNet [62]. FLOPs are calculated with the input size of 512×2048.

Mask R-CNN 1× schedule on COCO						Crop size 512×512 on ADE20K			
Backbone	AP^b	AP^m	#param.	FLOPs		Backbone	mIoU	#param.	FLOPs
Swin-T	42.7	39.3	48M	267G		ResNet-50	42.1	67M	953G
ConvNeXt-T	44.2	40.1	48M	262G		DeiT-S + MLN	43.8	58M	1217G
vHeat-T	45.1	41.0	53M	286G		Swin-T	44.4	60M	945G
Swin-S	44.8	40.9	69M	354G		Vim-S	44.9	46M	-
ConvNeXt-S	45.4	41.8	70M	348G		ConvNeXt-T	46.0	60M	939G
vHeat-S	46.8	42.3	74M	377G		vHeat-T	46.9	65M	969G
Swin-B	46.9	42.3	107M	496G		ResNet-101	43.8	86M	1030G
ConvNeXt-B	47.0	42.7	108M	486G		DeiT-B + MLN	45.5	144M	2007G
vHeat-B	47.7	43.0	115M	526G		Swin-S	47.6	81M	1039G
Mask R-CNN 3× MS schedule on COCO						NAT-S	48.0	82M	1010G
Swin-T	46.0	41.6	48M	267G		ConvNeXt-S	48.7	82M	1027G
ConvNeXt-T	46.2	41.7	48M	262G		vHeat-S	49.0	86M	1062G
vHeat-T	47.2	42.4	53M	286G		Swin-B	48.1	121M	1188G
Swin-S	48.2	43.2	69M	354G		NAT-B	48.5	123M	1137G
ConvNeXt-S	47.9	42.9	70M	348G		ConvNeXt-B	49.1	122M	1170G
vHeat-S	48.8	43.7	74M	377G		vHeat-B	49.6	129M	1219G

4 Experiment

Experiments are performed to assess vHeat and compare it against popular CNN and ViT models. Visualization analysis is presented to gain deeper insights into the mechanism of vHeat. The evaluation spans three vision tasks including image classification on ImageNet-1K, object detection on COCO, and semantic segmentation on ADE20K. Please refer to Sec. C for experimental settings.

4.1 Image Classification

The image classification results are summarized in Table 1. With similar FLOPs, vHeat-T achieves a top-1 accuracy of 82.2%, outperforming DeiT-S by 2.4%, and Swin-T by 0.9%, respectively. Notably,
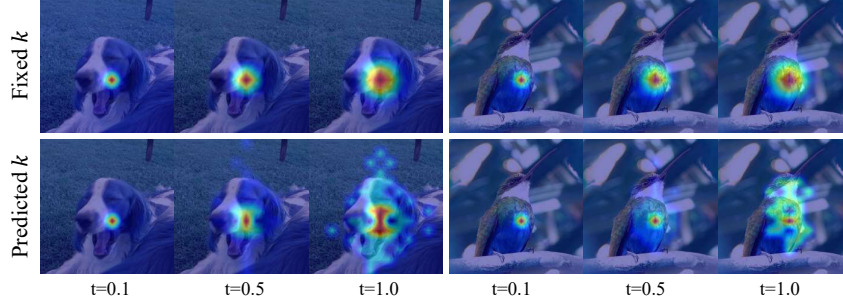
Figure 5: Temperature distribution (U^t) when using a randomly selected patch as the heat source. (Best viewed in color)

the superiority of vHeat is also observed at both Small and Base scales. Specifically, vHeat-B achieves a top-1 accuracy of 83.9%, outperforming DeiT-B by 2.1%, and Swin-B by 0.4%, respectively.

In terms of computational efficiency, vHeat enjoys significantly higher inference speed across Tiny/Small/Base model scales compared to benchmark models. For instance, vHeat-T achieves a throughput of 1514 image/s, 87% higher than Vim-S, 26% higher than ConvNeXt-T, and 22% higher than Swin-T, while maintaining a performance superiority, respectively.

4.2 Downstream Task

Object Detection and Instance Segmentation. As a backbone network, vHeat is tested on the MS COCO 2017 dataset [29] for object detection and instance segmentation. We load classification pre-trained vHeat weights for downstream evaluation. Considering the input image size is different from the classification task, the shape of FVEs or k should be aligned to the target image size on downstream tasks. Please refer to Sec. E.1 for ablation of interpolation for downstream tasks. The results for object detection are summarized in Table 2 (left), and vHeat enjoys superiority in box/mask Average Precision (AP^b and AP^m) in both of the training schedules (12 or 36 epochs). For example, with a 12-epoch fine-tuning schedule, vHeat-T/S/B models achieve object detection mAPs of $45.1\%/46.8\%/47.7\%$, outperforming Swin-T/S/B by $2.4\%/2.0\%/0.8\%$ mAP, and ConvNeXt-T/S/B by $0.9\%/1.4\%/0.7\%$ mAP, respectively. With the same configuration, vHeat-T/S/B achieve instance segmentation mAPs of $41.0\%/42.3\%/43.0\%$, outperforming Swin-T/S/B by $1.7\%/1.4\%/0.7\%$ mAP, and ConvNeXt-T/S/B by $0.9\%/0.5\%/0.3\%$ mAP, respectively. The advantages of vHeat persist under the 36-epoch ($3\times$) fine-tuning schedule with multi-scale training. These results showcase vHeat's potential to achieve promising performance in downstream tasks with dense prediction.

Semantic Segmentation. The results on ADE20K are summarized in Table 2 (right), and vHeat consistently achieves superior performance. For example, vHeat-B respectively outperform Swin-B [32] and ConvNeXt-B [33] by 1.5% and 0.5% mIoU.

4.3 Visualization Analysis

Visual Heat Conduction. In Fig. 5, we visualize the temperature U^t defined in Eq. (10) under predicted k when a random patch is taken as the heat source. With a predicted k, vHeat delivers self-adaptive visual heat conduction. With the increase of heat conduction time (t), the correlation of the selected patch to the whole image is enhanced. Please refer to Sec. F in Appendix for more visualization instances.

Receptive Field. The Effective Receptive Field (ERF) [36] of an output unit denotes the region of input that contains elements with a non-negligible influence on that unit. In Fig. 6, ResNet, ConNeXT, and Swin have local ERF. DeiT [52], HiViT [65], and vHeat exhibit global ERFs. The difference lies in that DeiT and HiViT have a $\mathcal{O}(N^2)$ complexity while vHeat enjoys $\mathcal{O}(N^{1.5})$ complexity.
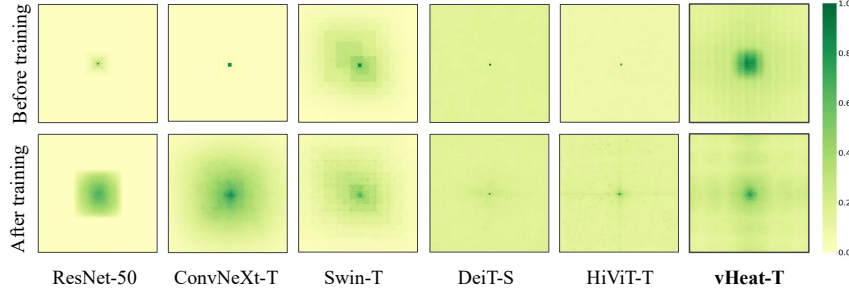
8

Figure 6: Visualization of the effective receptive fields (ERF) [36]. Pixels of higher intensity indicate larger responses with the central pixel.
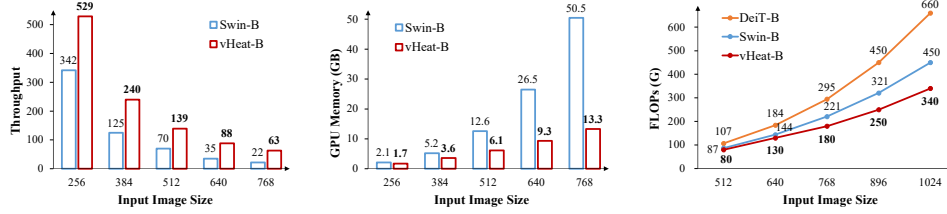

Figure 7: **Left / Mid / Right**: Throughput / GPU memory / FLOPs under different image resolutions. The throughput and GPU memory are tested on 80 GB Tesla A100 GPUs with batch size 64. Swin-B is tested with scaled window size here.

4.4 Computational Cost

The comparisons of throughput / GPU memory / FLOPs of vHeat-B and other ViTs are shown in Fig. 7. Thanks to HCO's $\mathcal{O}(N^{1.5})$ computational complexity $w.r.t.$ N image patches, vHeat-B has a significant superiority over other base-level ViT models on throughput / FLOPs. Fig. 7 (right) shows that with the increase of input image resolution, vHeat enjoys the slowest increase of computational overhead. Fig. 7 (middle) shows that vHeat requires 70% GPU memory less than Swin-Transformer given large input images. Given the larger image resolution, the superiority becomes larger. These demonstrate vHeat's great potential to handle high-resolution images.

4.5 Ablation of Thermal Diffusivity

To show the effectiveness of shared FVEs, we conduct the following experiments on ImageNet-1K. (1) Fix the thermal diffusivity $k = 0.0/1.0/10.0$. (2) Treat k as a learnable parameter for each layer. (3) Use individual FVEs to predict k for each layer. As shown in Table 3, when $k = 0.0$, the visual heat conduction doesn't work. A larger fixed k value, $e.g.$, $k = 5.0$, enables HCO to work isotropically without considering the image content and the performance reaches 81.7% top-1 accuracy. Predicting k by FVEs outperforms treating k as a learnable parameter, which may be attributed to the strengthened prior knowledge of frequency values provided by

Table 3: Evaluating thermal diffusivity k.

Settings	Acc
Fixed $k = 0.0$	81.0
Fixed $k = 1.0$	81.7
Fixed $k = 5.0$	81.8
k as a learnable parameter	81.5
Predicting k using individual FVEs	82.0
Predicting k using shared FVEs	**82.2**

FVEs. Please refer to Sec. E.5 in Appendix for the detailed analysis. When k is predicted by shared FVEs, the performance improves to 82.2%, which validates shared FVEs can effectively reduce the learning diffusivity and further improve the performance.

5 Conclusion

We propose vHeat, a visual backbone model that leverages the advantages of global receptive fields, low complexity, and interoperability. The effectiveness of the vHeat model family, including

vHeat-T/S/B models, has been demonstrated through extensive experiments and ablation studies, significantly outperforming popular CNNs and ViTs. The results highlight the potential of vHeat as a new paradigm for vision representation learning, offering fresh insights for the development of physics-inspired vision models.

Limitations. Based on the physical heat conduction, the learning process of vHeat may become challenging when distant information conduction is required, as it needs extensive training to effectively perceive long-range dependencies. Moreover, masked image modeling serves as an effective self-supervised learning paradigm for ViTs. By now, we have not yet developed a self-supervised learning method for vHeat, which is left for the future work.

References

[1] Alaaeldin Ali, Hugo Touvron, Mathilde Caron, Piotr Bojanowski, Matthijs Douze, Armand Joulin, Ivan Laptev, Natalia Neverova, Gabriel Synnaeve, Jakob Verbeek, et al. Xcit: Cross-covariance image transformers. *NeurIPS*, 34:20014–20027, 2021.

[2] Priyanka Bawane, Snehali Gadariye, S Chaturvedi, and AA Khurshid. Object and character recognition using spiking neural network. *Materials Today: Proceedings*, 5(1):360–366, 2018.

[3] R Byron Bird. Transport phenomena. *Appl. Mech. Rev.*, 55(1):R1–R4, 2002.

[4] Chun-Fu Chen, Quanfu Fan, and Rameswar Panda. Crossvit: Cross-attention multi-scale vision transformer for image classification. In *ICCV*, 2021.

[5] Kai Chen, Jiaqi Wang, Jiangmiao Pang, Yuhang Cao, Yu Xiong, Xiaoxiao Li, Shuyang Sun, Wansen Feng, Ziwei Liu, Jiarui Xu, Zheng Zhang, Dazhi Cheng, Chenchen Zhu, Tianheng Cheng, Qijie Zhao, Buyu Li, Xin Lu, Rui Zhu, Yue Wu, Jifeng Dai, Jingdong Wang, Jianping Shi, Wanli Ouyang, Chen Change Loy, and Dahua Lin. Mmdetection: Open mmlab detection toolbox and benchmark. *arXiv preprint arXiv:1906.07155*, 2019.

[6] Yinpeng Chen, Xiyang Dai, Dongdong Chen, Mengchen Liu, Lu Yuan, Zicheng Liu, and Youzuo Lin. Self-supervised learning based on heat equation. *arXiv preprint arXiv:2211.13228*, 2022.

[7] Alexander H-D Cheng and Daisy T Cheng. Heritage and early history of the boundary element method. *Engineering analysis with boundary elements*, 29(3):268–302, 2005.

[8] François Chollet. Xception: Deep learning with depthwise separable convolutions. In *CVPR*, pages 1251–1258, 2017.

[9] Jifeng Dai, Haozhi Qi, Yuwen Xiong, Yi Li, Guodong Zhang, Han Hu, and Yichen Wei. Deformable convolutional networks. In *ICCV*, pages 764–773, 2017.

[10] Zihang Dai, Hanxiao Liu, Quoc V Le, and Mingxing Tan. Coatnet: Marrying convolution and attention for all data sizes. *NeurIPS*, 34:3965–3977, 2021.

[11] Sybren Ruurds De Groot and Peter Mazur. *Non-equilibrium thermodynamics*. Courier Corporation, 2013.

[12] Jia Deng, Wei Dong, Richard Socher, Li-Jia Li, Kai Li, and Fei-Fei Li. Imagenet: A large-scale hierarchical image database. In *CVPR*, pages 248–255, 2009.

[13] Mingyu Ding, Bin Xiao, Noel Codella, Ping Luo, Jingdong Wang, and Lu Yuan. Davit: Dual attention vision transformers. In *ECCV*, pages 74–92, 2022.

[14] Xiaohan Ding, Xiangyu Zhang, Jungong Han, and Guiguang Ding. Scaling up your kernels to 31×31: Revisiting large kernel design in cnns. In *CVPR*, pages 11953–11965, 2022.

[15] Xiaoyi Dong, Jianmin Bao, Dongdong Chen, Weiming Zhang, Nenghai Yu, Lu Yuan, Dong Chen, and Baining Guo. Cswin transformer: A general vision transformer backbone with cross-shaped windows. In *CVPR*, pages 12124–12134, 2022.

[16] Alexey Dosovitskiy, Lucas Beyer, Alexander Kolesnikov, Dirk Weissenborn, Xiaohua Zhai, Thomas Unterthiner, Mostafa Dehghani, Matthias Minderer, Georg Heigold, Sylvain Gelly, Jakob Uszkoreit, and Neil Houlsby. An image is worth 16x16 words: Transformers for image recognition at scale. In *ICLR*, 2021.

[17] Jonas Gehring, Michael Auli, David Grangier, Denis Yarats, and Yann N Dauphin. Convolutional sequence to sequence learning. In *ICML*, pages 1243–1252. PMLR, 2017.

[18] Samanwoy Ghosh-Dastidar and Hojjat Adeli. Spiking neural networks. *International journal of neural systems*, 19(04):295–308, 2009.

[19] Albert Gu and Tri Dao. Mamba: Linear-time sequence modeling with selective state spaces. *arXiv preprint arXiv:2312.00752*, 2023.

[20] Albert Gu, Karan Goel, Ankit Gupta, and Christopher Ré. On the parameterization and initialization of diagonal state space models. *NeurIPS*, 35:35971–35983, 2022.

[21] Kaiming He, Xiangyu Zhang, Shaoqing Ren, and Jian Sun. Deep residual learning for image recognition. In *CVPR*, pages 770–778, 2016.

[22] Jonathan Ho, Ajay Jain, and Pieter Abbeel. Denoising diffusion probabilistic models. *NeurIPS*, 33:6840–6851, 2020.

[23] Andrew G Howard, Menglong Zhu, Bo Chen, Dmitry Kalenichenko, Weijun Wang, Tobias Weyand, Marco Andreetto, and Hartwig Adam. Mobilenets: Efficient convolutional neural networks for mobile vision applications. *arXiv preprint arXiv:1704.04861*, 2017.

[24] Binh-Son Hua, Minh-Khoi Tran, and Sai-Kit Yeung. Pointwise convolutional neural networks. In *CVPR*, pages 984–993, 2018.

[25] Gao Huang, Zhuang Liu, Laurens Van Der Maaten, and Kilian Q Weinberger. Densely connected convolutional networks. In *CVPR*, pages 4700–4708, 2017.

[26] Alex Krizhevsky, Ilya Sutskever, and Geoffrey E. Hinton. Imagenet classification with deep convolutional neural networks. In *NeurIPS*, pages 1106–1114, 2012.

[27] Yann LeCun, Léon Bottou, Yoshua Bengio, and Patrick Haffner. Gradient-based learning applied to document recognition. *Proceedings of the IEEE*, 86(11):2278–2324, 1998.

[28] Jun Haeng Lee, Tobi Delbruck, and Michael Pfeiffer. Training deep spiking neural networks using backpropagation. *Frontiers in neuroscience*, 10:228000, 2016.

[29] Tsung-Yi Lin, Michael Maire, Serge J. Belongie, James Hays, Pietro Perona, Deva Ramanan, Piotr Dollár, and C. Lawrence Zitnick. Microsoft COCO: common objects in context. In *ECCV*, pages 740–755, 2014.

[30] Yue Liu, Yunjie Tian, Yuzhong Zhao, Hongtian Yu, Lingxi Xie, Yaowei Wang, Qixiang Ye, and Yunfan Liu. Vmamba: Visual state space model. *arXiv preprint arXiv:2401.10166*, 2024.

[31] Ze Liu, Han Hu, Yutong Lin, Zhuliang Yao, Zhenda Xie, Yixuan Wei, Jia Ning, Yue Cao, Zheng Zhang, Li Dong, et al. Swin transformer v2: Scaling up capacity and resolution. In *CVPR*, pages 12009–12019, 2022.

[32] Ze Liu, Yutong Lin, Yue Cao, Han Hu, Yixuan Wei, Zheng Zhang, Stephen Lin, and Baining Guo. Swin transformer: Hierarchical vision transformer using shifted windows. In *ICCV*, pages 10012–10022, 2021.

[33] Zhuang Liu, Hanzi Mao, Chao-Yuan Wu, Christoph Feichtenhofer, Trevor Darrell, and Saining Xie. A convnet for the 2020s. In *CVPR*, pages 11976–11986, 2022.

[34] Ilya Loshchilov and Frank Hutter. Decoupled weight decay regularization. *arXiv preprint arXiv:1711.05101*, 2017.

[35] Jiasen Lu, Roozbeh Mottaghi, Aniruddha Kembhavi, et al. Container: Context aggregation networks. *NeurIPS*, 34:19160–19171, 2021.

[36] Wenjie Luo, Yujia Li, Raquel Urtasun, and Richard Zemel. Understanding the effective receptive field in deep convolutional neural networks. *NeurIPS*, 29, 2016.

[37] Eric Nguyen, Karan Goel, Albert Gu, Gordon Downs, Preey Shah, Tri Dao, Stephen Baccus, and Christopher Ré. S4nd: Modeling images and videos as multidimensional signals with state spaces. *NeurIPS*, 35:2846–2861, 2022.

[38] Bo Peng, Eric Alcaide, Quentin Anthony, Alon Albalak, Samuel Arcadinho, Stella Biderman, Huanqi Cao, Xin Cheng, Michael Chung, Leon Derczynski, Xingjian Du, Matteo Grella, Kranthi Gv, Xuzheng He, Haowen Hou, Przemyslaw Kazienko, Jan Kocon, Jiaming Kong, Bartlomiej Koptyra, Hayden Lau, Jiaju Lin, Krishna Sri Ipsit Mantri, Ferdinand Mom, Atsushi Saito, Guangyu Song, Xiangru Tang, Johan S. Wind, Stanislaw Wozniak, Zhenyuan Zhang, Qinghua Zhou, Jian Zhu, and Rui-Jie Zhu. RWKV: reinventing rnns for the transformer era. In Houda Bouamor, Juan Pino, and Kalika Bali, editors, *EMNLP*, pages 14048–14077, 2023.

[39] Zhiliang Peng, Li Dong, Hangbo Bao, Qixiang Ye, and Furu Wei. Beit v2: Masked image modeling with vector-quantized visual tokenizers. *arXiv preprint arXiv:2208.06366*, 2022.

[40] Ilija Radosavovic, Raj Prateek Kosaraju, Ross Girshick, Kaiming He, and Piotr Dollár. Designing network design spaces. In *CVPR*, pages 10428–10436, 2020.

[41] Yongming Rao, Wenliang Zhao, Zheng Zhu, Jiwen Lu, and Jie Zhou. Global filter networks for image classification. *NeurIPS*, 34:980–993, 2021.

[42] Chitwan Saharia, William Chan, Saurabh Saxena, Lala Li, Jay Whang, Emily L Denton, Kamyar Ghasemipour, Raphael Gontijo Lopes, Burcu Karagol Ayan, Tim Salimans, et al. Photorealistic text-to-image diffusion models with deep language understanding. *NeurIPS*, 35:36479–36494, 2022.

[43] Karen Simonyan and Andrew Zisserman. Very deep convolutional networks for large-scale image recognition. *arXiv preprint arXiv:1409.1556*, 2014.

[44] Jiaming Song, Chenlin Meng, and Stefano Ermon. Denoising diffusion implicit models. *arXiv preprint arXiv:2010.02502*, 2020.

[45] Aravind Srinivas, Tsung-Yi Lin, Niki Parmar, Jonathon Shlens, Pieter Abbeel, and Ashish Vaswani. Bottleneck transformers for visual recognition. In *CVPR*, pages 16519–16529, 2021.

[46] Gilbert Strang. The discrete cosine transform. *SIAM review*, 41(1):135–147, 1999.

[47] Yutao Sun, Li Dong, Shaohan Huang, Shuming Ma, Yuqing Xia, Jilong Xue, Jianyong Wang, and Furu Wei. Retentive network: A successor to transformer for large language models. *arXiv preprint arXiv:2307.08621*, 2023.

[48] Christian Szegedy, Wei Liu, Yangqing Jia, Pierre Sermanet, Scott Reed, Dragomir Anguelov, Dumitru Erhan, Vincent Vanhoucke, and Andrew Rabinovich. Going deeper with convolutions. In *CVPR*, pages 1–9, 2015.

[49] Mingxing Tan and Quoc V. Le. Efficientnet: Rethinking model scaling for convolutional neural networks. In *ICML*, pages 6105–6114, 2019.

[50] Amirhossein Tavanaei, Masoud Ghodrati, Saeed Reza Kheradpisheh, Timothée Masquelier, and Anthony Maida. Deep learning in spiking neural networks. *Neural networks*, 111:47–63, 2019.

[51] Yunjie Tian, Lingxi Xie, Zhaozhi Wang, Longhui Wei, Xiaopeng Zhang, Jianbin Jiao, Yaowei Wang, Qi Tian, and Qixiang Ye. Integrally pre-trained transformer pyramid networks. In *CVPR*, pages 18610–18620, 2023.

[52] Hugo Touvron, Matthieu Cord, Matthijs Douze, Francisco Massa, Alexandre Sablayrolles, and Hervé Jégou. Training data-efficient image transformers & distillation through attention. In *ICML*, pages 10347–10357, 2021.

[53] Ashish Vaswani, Prajit Ramachandran, Aravind Srinivas, Niki Parmar, Blake Hechtman, and Jonathon Shlens. Scaling local self-attention for parameter efficient visual backbones. In *CVPR*, pages 12894–12904, 2021.

[54] Ashish Vaswani, Noam Shazeer, Niki Parmar, Jakob Uszkoreit, Llion Jones, Aidan N Gomez, Łukasz Kaiser, and Illia Polosukhin. Attention is all you need. In *NeurIPS*, 2017.

[55] Jue Wang, Wentao Zhu, Pichao Wang, Xiang Yu, Linda Liu, Mohamed Omar, and Raffay Hamid. Selective structured state-spaces for long-form video understanding. In *CVPR*, pages 6387–6397, 2023.

[56] Sinong Wang, Belinda Z Li, Madian Khabsa, Han Fang, and Hao Ma. Linformer: Self-attention with linear complexity. *arXiv preprint arXiv:2006.04768*, 2020.

[57] Wenhai Wang, Jifeng Dai, Zhe Chen, Zhenhang Huang, Zhiqi Li, Xizhou Zhu, Xiaowei Hu, Tong Lu, Lewei Lu, Hongsheng Li, Xiaogang Wang, and Yu Qiao. Internimage: Exploring large-scale vision foundation models with deformable convolutions. In *CVPR*, pages 14408–14419, 2023.

[58] Wenhai Wang, Enze Xie, Xiang Li, Deng-Ping Fan, Kaitao Song, Ding Liang, Tong Lu, Ping Luo, and Ling Shao. Pyramid vision transformer: A versatile backbone for dense prediction without convolutions. In *ICCV*, pages 568–578, 2021.

[59] Wenhai Wang, Enze Xie, Xiang Li, Deng-Ping Fan, Kaitao Song, Ding Liang, Tong Lu, Ping Luo, and Ling Shao. Pvt v2: Improved baselines with pyramid vision transformer. *Computational Visual Media*, 8(3):415–424, 2022.

[60] David Vernon Widder. *The heat equation*, volume 67. Academic Press, 1976.

[61] Ross Wightman. Pytorch image models. `https://github.com/rwightman/pytorch-image-models`, 2019.

[62] Tete Xiao, Yingcheng Liu, Bolei Zhou, Yuning Jiang, and Jian Sun. Unified perceptual parsing for scene understanding. In *ECCV*, pages 418–434, 2018.

[63] Jianwei Yang, Chunyuan Li, Pengchuan Zhang, Xiyang Dai, Bin Xiao, Lu Yuan, and Jianfeng Gao. Focal self-attention for local-global interactions in vision transformers. *arXiv preprint arXiv:2107.00641*, 2021.

[64] Fisher Yu and Vladlen Koltun. Multi-scale context aggregation by dilated convolutions. *arXiv preprint arXiv:1511.07122*, 2015.

[65] Xiaosong Zhang, Yunjie Tian, Lingxi Xie, Wei Huang, Qi Dai, Qixiang Ye, and Qi Tian. Hivit: A simpler and more efficient design of hierarchical vision transformer. In *ICLR*, 2023.

[66] Weixi Zhao, Weiqiang Wang, and Yunjie Tian. Graformer: Graph-oriented transformer for 3d pose estimation. In *CVPR*, pages 20438–20447, 2022.

[67] Lianghui Zhu, Bencheng Liao, Qian Zhang, Xinlong Wang, Wenyu Liu, and Xinggang Wang. Vision mamba: Efficient visual representation learning with bidirectional state space model. *arXiv preprint arXiv:2401.09417*, 2024.

A Motivation

Modern visual representation models are built upon the attention mechanism inspired by biological vision systems. One drawback of it is the lack of a clear definition of the relationship between biological electrical signals and brain activity (energy). This drives us to break through the attention mechanism and attempt other physical laws. Heat conduction is a physical phenomenon in nature, characterized by the propagation of energy. The heat conduction process combines implicit attention computation with energy computation and has the potential to be a new mechanism for visual representation models.

B HCO implementation using $\mathbf{DCT_{2D}}$ and $\mathbf{IDCT_{2D}}$

Assume a matrix denoted as $\mathbf{A}$ and the transformed matrix denoted as $\mathbf{B}$, the $\mathbf{DCT_{2D}}$ and the $\mathbf{IDCT_{2D}}$ can be performed by

$$
\begin{aligned}
\mathbf{DCT_{2D}} : \mathbf{B}_{pq} &= \alpha_{\mathbf{p}}\alpha_{\mathbf{q}} \sum_{m=0}^{M-1} \sum_{n=0}^{N-1} \mathbf{A}_{mn} \cos\frac{(2m+1)p\pi}{2M} \cos\frac{(2n+1)q\pi}{2N}, \\
\mathbf{IDCT_{2D}} : \mathbf{A}_{mn} &= \sum_{m=0}^{M-1} \sum_{n=0}^{N-1} \alpha_{\mathbf{p}}\alpha_{\mathbf{q}} \mathbf{B}_{pq} \cos\frac{(2m+1)p\pi}{2M} \cos\frac{(2n+1)q\pi}{2N},
\end{aligned}
\tag{11}
$$

where $0 \leq \{p, m\} \leq M - 1$, $0 \leq \{q, n\} \leq N - 1$, $\alpha_{\mathbf{p}} = \begin{cases} \dfrac{1}{\sqrt{M}}, p = 0 \\ \dfrac{2}{\sqrt{M}}, p > 0 \end{cases}$, and $\alpha_{\mathbf{q}} = \begin{cases} \dfrac{1}{\sqrt{N}}, q = 0 \\ \dfrac{2}{\sqrt{N}}, q > 0 \end{cases}$. M and N respectively denote the row and column sizes of $\mathbf{A}$. Considering the matrix multiplication is GPU-friendly, we implement the $\mathbf{DCT_{2D}}$ and $\mathbf{IDCT_{2D}}$ in Eq. (11) by

$$
\begin{aligned}
\mathbf{C} &= (\mathbf{C}_{mp})_{M \times M} = \left(\alpha_{\mathbf{p}} \cos\frac{(2m+1)p\pi}{2M} \right)_{M \times M}, \\
\mathbf{D} &= (\mathbf{D}_{nq})_{N \times N} = \left(\alpha_{\mathbf{q}} \cos\frac{(2n+1)q\pi}{2N} \right)_{N \times N}, \\
\mathbf{B} &= \mathbf{CAD^T}, \\
\mathbf{A} &= \mathbf{C^TBD}.
\end{aligned}
\tag{12}
$$

Suppose the number of total patches is N and the image is square, the shapes of $\mathbf{A}$, $\mathbf{B}$, $\mathbf{C}$ and $\mathbf{D}$ are all $\sqrt{N} \times \sqrt{N}$, which illustrates the computational complexity of (12) and HCO is $O(N^{1.5})$.

C Experimental Settings

Model configurations. The configurations of vHeat-T/S/B models are shown in Table 4.

Table 4: Configurations of vHeat. The contents in the tuples represent configurations for four stages.

Size	Tiny	Small	Base
Stem	3×3 conv with stride 2; Norm; GELU; 3×3 conv with stride 2; Norm		
Downsampling	3×3 conv with stride 2; Norm		
MLP ratio	4		
Classifier head	Global average pooling, Norm, MLP		
Layers	(2, 2, 6, 2)	(2, 2, 18, 2)	(2, 2, 18, 2)
Channels	(96, 192, 384, 768)	(96, 192, 384, 768)	(128, 256, 512, 1024)

Image Classification. Following the standard evaluation protocol used in [31], all vHeat series are trained from scratch for 300 epochs and warmed up for the first 20 epochs. We utilize the AdamW

optimizer [34] during the training process with betas set to $(0.9, 0.999)$, a momentum of 0.9, a cosine decay learning rate scheduler, an initial learning rate of 2×10^{-3}, a weight decay of 0.08, and a batch size of 2048. The drop path rates are set to $0.1/0.3/0.5$ for vHeat-T/S/B, respectively. Other techniques such as label smoothing (0.1) and exponential moving average (EMA) are also applied. No further training techniques are employed beyond these for a fair comparison. The training of vHeat-T/S/B takes 5/7/8.5 minutes per epoch on Tesla 16×V100 GPUs.

object Detection. Following the settings in Swin [31] with the Mask-RCNN detector, we build the vHeat-based detector using the MMDetection library [5]. The AdamW optimizer [34] with a batch size of 16 is used to train the detector. The initial learning rate is set to 1×10^{-4} and is reduced by a factor of $10\times$ at the 9th and 11th epoch. The fine-tune process takes 12 (1×) or 36 (3×) epochs. We employ the multi-scale training and random flip technique, which aligns with the established practices for object detection evaluations.

Semantic Segmentation. Following the setting of Swin Transfomer [32], we construct a Uper-Head [62] on top of the pre-trained vHeat model to test its capability for semantic segmentation. The AdamW optimizer [34] is employed and the learning rate is set to 6×10^{-5} with a batch size of 16. The fine-tuning process takes a total of standard $160k$ iterations and the default input resolution is 512×512.

D   Performance Comparison

The complete comparison of vHeat and other vision models on ImageNet-1K is shown in Table 5.

Table 5: **Performance comparison of image classification on ImageNet-1K**.

Method	Image size	#Param.	FLOPs	Test Throughput (img/s)	ImageNet top-1 acc. (%)
DeiT-S [52]	224^2	22M	4.6G	1761	79.8
DeiT-B [52]	224^2	86M	17.5G	503	81.8
ConvNeXt-T [33]	224^2	29M	4.5G	1198	82.1
ConvNeXt-S [33]	224^2	50M	8.7G	684	83.1
ConvNeXt-B [33]	224^2	89M	15.4G	436	83.8
HiViT-T [65]	224^2	19M	4.6G	1393	82.1
HiViT-S [65]	224^2	38M	9.1G	712	83.5
HiViT-B [65]	224^2	66M	15.9G	456	83.8
XCiT-S/12 [1]	224^2	26M	4.8G	1283	82.0
XCiT-S/24 [1]	224^2	48M	9.1G	671	82.6
XCiT-M/24 [1]	224^2	84M	16.2G	423	82.7
Vim-S [67]	224^2	26M	-	811	80.5
Swin-T [32]	224^2	28M	4.6G	1244	81.3
Swin-S [32]	224^2	50M	8.7G	718	83.0
Swin-B [32]	224^2	88M	15.4G	458	83.5
vHeat-T	224^2	29M	4.6G	1514	82.2
vHeat-S	224^2	50M	8.5G	945	83.6
vHeat-B	224^2	87M	14.9G	661	83.9

E   Additional Ablation Studies

E.1   Interpolation of FVEs/k for downstream tasks

We have tried several approaches to align the shape for ablation. (1) Directly interpolate FVEs to the target shape of the input image. (2) Add 0 to the lower right region of FVEs to align the target shape. (3) Add 0 to the lower right region of FVEs to 512×512, and interpolate to the target shape. (4)

Table 6: Evaluating different methods to align the shape of FVEs/k when loading ImageNet-1K pre-trained vHeat-B weights for detection and segmentation on COCO.

Method	AP^b	AP^m
Interpolating FVEs to predict k	47.4	42.9
Adding 0 to FVEs	47.4	42.7
Adding 0, then interpolating FVEs	**47.7**	**43.0**
Interpolating the predicted k	47.2	42.7

Directly interpolate the predicted thermal diffusivity k to the target shape. The results are summarized in Table 6. Through the comparison, we select adding 0, then interpolating FVEs to the target shape for all downstream tasks.

E.2 Plain vHeat model

We've tested the performance of plain vHeat-B on ImageNet-1K classification. Keeping the same as DeiT-B, plain vHeat-B has 12 HCO layers, 768 embedding channels and the patch size is set to 16. Results are shown in Table 7. The superiority of plain vHeat-B over DeiT-B also validates the effectiveness of vHeat model.

Table 7: Evaluating different methods to align the shape of FVEs when loading ImageNet-1K pre-trained vHeat-B weights for detection and segmentation on COCO.

Model	#Param.	FLOPs	Acc
DeiT-B	86M	17.5G	81.8
Plain vHeat-B	88M	16.9G	**82.6**

E.3 Depth-wise convolution

We conduct experiments to validate the performance improvement from DWConv. We replace depth-wise convolution with layer normalization for vHeat-B. Results are summarized in Table 8, and vHeat-B achieves 83.7% Top-1 accuracy on ImageNet-1K classification, 0.2% lower than with DWConv, which validates the main gains come from the proposed HCO. Besides, when k is fixed as a large value, e.g. $k = 10.0$, replacing DWConv with layer normalization causes a significant performance drop (-0.7% top-1 accuracy). The comparison validates predicting k by FVEs can effectively improve the robustness of vHeat.

Additionally, we train vHeat without DWConv with a different recipe from vHeat with DWConv. The batch size is set as 1024, the initial learning rate is set as 1×10^{-3}, and the weight decay is set as 0.05.

Table 8: Ablation experiments of depth-wise convolution (DWConv).

Model	DWConv	Acc
vHeat-B	✓	83.9
vHeat-B	✗	83.7 (-0.2)
vHeat-B (fix k=10.0)	✓	83.5
vHeat-B (fix k=10.0)	✗	82.8 (-0.7)

E.4 Global filters

Considering HCO works as a global filter in the frequency domain for visual heat conduction, we compare vHeat with (1) GFNet [41], and (2) replacing HCO with the operators proposed in GFNet for

ablation. Results are summarized in Table 9, vHeat-S has a large superiority over GFNet-H-B under approximate model scale. Besides, replacing HCO with operations proposed in GFNet achieves lower performance, which validates the effectiveness of the proposed HCO and visual heat conduction modeling for representation.

Table 9: Comparison of vHeat with global filters, where vHeat-B* denotes replacing HCO with operators proposed in GFNet.

Model	#Param.	FLOPs	Acc
vHeat-S	50M	8.5G	83.6
GFNet-H-B [41]	54M	8.4G	82.9
vHeat-B	87M	14.9G	83.9
vHeat-B*	87M	14.9G	83.5

E.5 Predicting k by FVEs *vs.* treating k as a learnable parameter

After performing DCT, the features lack explicit frequency value, while FVEs provide the model with prior knowledge of frequency values. Similar to how the introduction of positional encoding can enhance performance even in models that include positional information [17], predicting k by FVEs, rather than treating k as a learnable parameter, reinforces prior frequency information and more clearly represents the relationship between frequency and thermal diffusivity.

F Heat Conduction Visualization

We visualize more instances of visual heat conduction, given a randomly selected patch as the heat source, Fig. 8, validating the self-adaptive visual heat conduction pattern through the prediction of k.
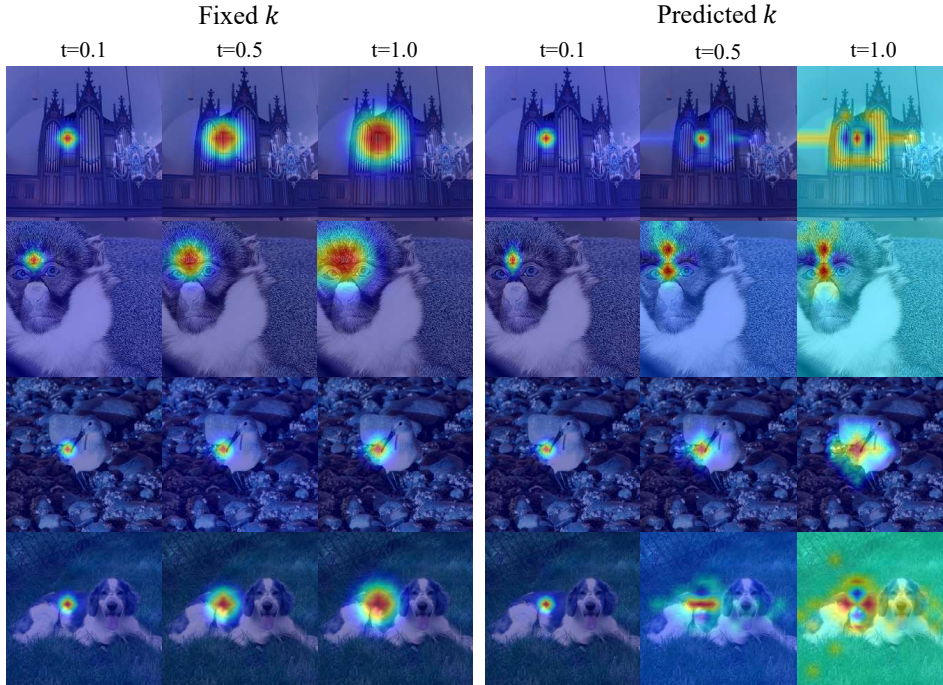

Figure 8: Temperature distribution (U^t) when using a randomly selected patch as the heat source. (Best viewed in color)

G Feature Map Visualization

We visualize the feature before/after HCO in a random layer in stage 2 with randomly selected images as input, Fig. 9. Before HCO, only a few regions of the foreground object are activated. After HCO, almost the entire foreground object is activated intensively.

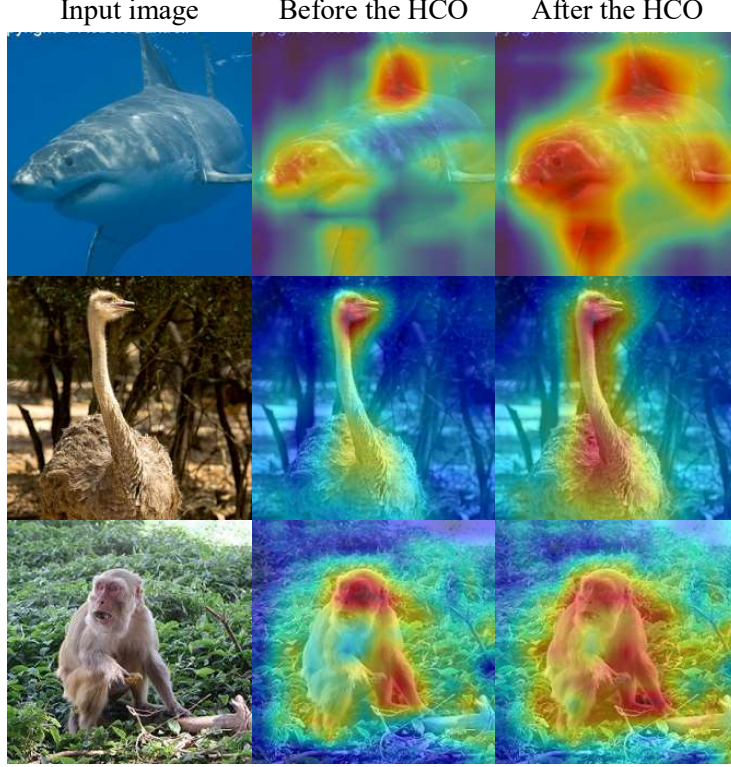Input image   Before the HCO   After the HCO

Figure 9: Visualization of the feature before/after HCO in a random layer in stage 2 with ImageNet-1K classification pre-trained vHeat-B. The images are randomly selected from ImageNet-1K.

H Analysis of k in each layer

We calculate average values of k in each layer of ImageNet-1K classification pre-trained vHeat-Tiny, Fig. 10. In stage 2 and stage 3, average values of k corresponding to deeper layers are larger, indicating that the visual heat conduction effect of deeper layers is stronger, leading to faster and farther overall content propagation.
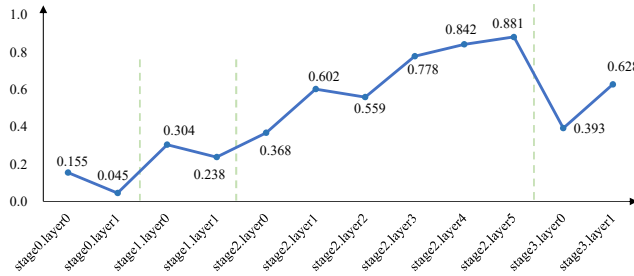

Figure 10: Average values of k in each layer.